

RESEARCH ACTIVITIES VIII

Laser Research Center for Molecular Science

VIII-A Developments and Researches of New Laser Materials

Although development of lasers is remarkable, there are no lasers which lase in ultraviolet and far infrared regions. However, it is expected that these kinds of lasers break out a great revolution in not only the molecular science but also in the industrial world.

In this project we research characters of new materials for ultraviolet and far infrared lasers, and develop new lasers by using these laser materials.

VIII-A-1 Intense THz Radiation from Femtosecond Laser Pulses Irradiated InAs in a Strong Magnetic Field

OHTAKE, Hideyuki; ONO, Shingo¹; KAWAHATA, Eiji; LIU, Zhenlin; SARUKURA, Nobuhiko
(¹Sci. Univ. Tokyo)

Since the first observation of THz radiation from InAs surface irradiated with femtosecond laser pulses, considerable effort have been made to design an intense THz-radiation source and to understand the mechanism for generating THz radiation. However, the problem has not been solved. In this paper, we have investigated the intense THz radiation from InAs by applying a strong magnetic field up to 5 T. We compared several different geometries. Besides quadratic magnetic field dependence, we found saturation of the THz-radiation intensity around 3 T. Furthermore, the intensity decreased dramatically above 3 T. It represented that the most suitable magnetic field was 3 T to design an intense THz-radiation source. We also took spectra by a Polarizing Michelson interferometer. The spectral shapes for the different magnetic field directions were significantly different. The center frequency of these spectra shifted to lower frequency with increasing magnetic field. Through these experiments, we found the best configuration and the most suitable magnetic field to obtain an intense THz radiation for various applications such as imaging, sensing, and spectroscopy. This configuration dependence of the spectral shape and the center frequency is attributed to be the initial carrier acceleration processes modulated by a strong magnetic field.

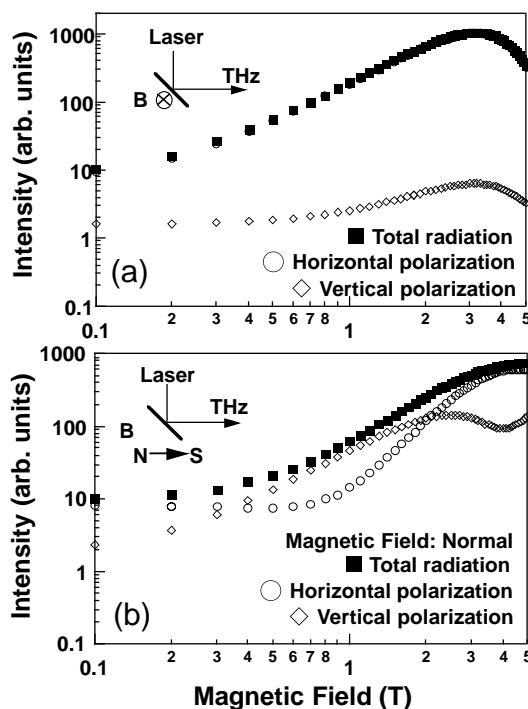


Figure 1. Magnetic field dependence of THz-radiation intensity. Inset indicates the experimental geometry. Closed squares, open circle and diamonds show total radiation, horizontal and vertical polarization, respectively. (a) The saturation of THz radiation intensity is clearly observed. (b) The saturation is not observed.

VIII-A-2 High-Repetition-Rate, High-Average-Power Mode-Locked Ti:Sapphire Laser with an Intracavity cw-Amplification Scheme

LIU, Zhenlin; ONO, Shingo¹; KOZEKI, Toshimasa; OHTAKE, Hideyuki; SARUKURA, Nobuhiko
(¹Sci. Univ. Tokyo)

We have demonstrated a high-average-power, mode-locked Ti:sapphire laser with an intracavity cw-amplification scheme. The laser generated 150-fs pulses with 3.4-W average power at a repetition rate of 79 MHz. This simple amplification scheme can be applied for the power scaling of other lasers.

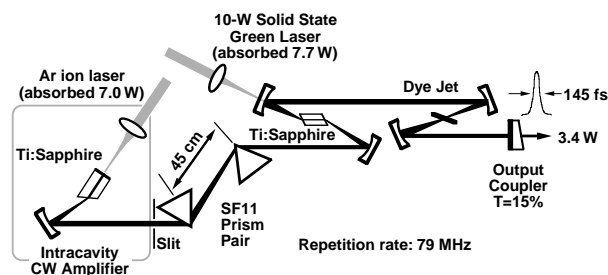


Figure 1. Configuration of high-repetition-rate high-average-power (3.4 W) femtosecond Ti:sapphire laser with an intracavity cw amplifier. The half-cut Brewster Ti:sapphire crystal composed the intracavity cw amplifier.

VIII-A-3 Compact THz-radiation Source Consisting of a Bulk Semiconductor, a Mode-Locked Fiber Laser, and a 2-T Permanent Magnet

ONO, Shingo¹; TSUKAMOTO, Takeyo¹; KAWAHATA, Eiji; LIU, Zhenlin; OHTAKE, Hideyuki; SARUKURA, Nobuhiko; NISHIZAWA, Seizi²; NAKANISHI, Akio³; YOSHIDA, Makoto⁴
 (¹Sci. Univ. Tokyo; ²JASCO Corporation; ³Sumitomo Special Metals co., Ltd; ⁴IMRA AMERICA, INC. JLO)

Various THz-radiation sources have been intensively studied including photo conductive switches irradiated with ultrashort optical pulses. An intense, compact, and simple light source is required for applications in sensing or imaging. We have demonstrated the strong enhancement of THz-radiation power with a magnetic field by using an InAs semiconductor. In this paper, we report on a compact THz-radiation source consisting of a fiber femtosecond laser and a newly designed 2-T permanent magnet shown in Figure 1. A mode-locked frequency doubled Er-doped fiber laser delivered 170-fsec pulses at 780 nm with a 48.5-MHz repetition rate (IMRA model FA7850/10SA) with 30-mW average power and 4.1-kW peak power. The mode-locked fiber laser is a completely turn-key system. It is much smaller than a mode-locked Ti:sapphire laser that requires daily alignment. The used semiconductor sample was undoped bulk InAs with a (100) surface. The 2-T permanent magnet unit consisted of 8 Nd-Fe-B magnet pieces. The remanence magnetic field of the Nd-Fe-B material itself was 1.3 T (NEOMAX-44H). Owing to the new magnetic circuit design, the magnetic field in the center exceeded the remanence magnetic field of the material. The permanent magnet only weighs about 5 kg. The 2-T permanent magnet unit is smaller and much lighter than an electromagnet. At present the average power is estimated to sub-micro watt level. The spectra of the THz radiation were obtained by a Polarizing Michelson interferometer. Many water vapor absorption lines were clearly observed. Therefore, the THz-radiation source is already usable for spectroscopy. Such a simple and compact source will open up new application for THz-radiation.

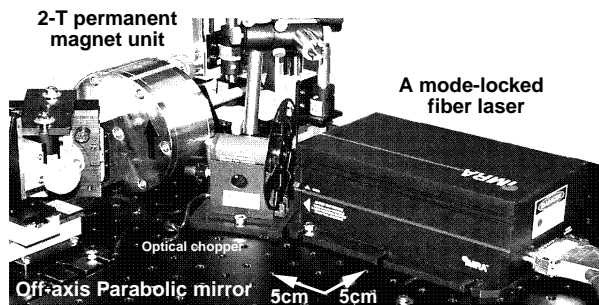


Figure 1. Photograph of a compact THz-radiation source with a bulk semiconductor, a fiber femtosecond laser, and a 2-T permanent magnet. Including the laser, the size is less than 40 × 30 × 15 cm.

VIII-A-4 Spectrum Control of THz Radiation from InAs in a Magnetic Field by Duration and Frequency Chirp of the Excitation Pulses

SUZUKI, Yuji; ONO, Shingo¹; LIU, Zhenlin; OHTAKE, Hideyuki; SARUKURA, Nobuhiko
 (¹Sci. Univ. Tokyo)

The THz-radiation spectrum from InAs in a magnetic field irradiated with femtosecond pulses can be controlled by varying the excitation pulse width and chirp direction of the excitation pulse. A longer excitation pulse width produces lower frequency THz radiation. Also, positively chirped pulse excitation will generate higher power and higher frequency THz radiation, due to the corruption of the impulse response of the semiconductor in the longer pulse width region. The spectral shape of the radiation strongly depends on the chirp direction. This unexpected difference with the same excitation peak power and the same pulse duration with different chirp direction is rather surprising. This difference of THz-radiation for the chirping of the excitation pulses might be attributed to the difference of the photo-carrier relaxation process in the conduction band with oppositely chirped-pulse excitation.

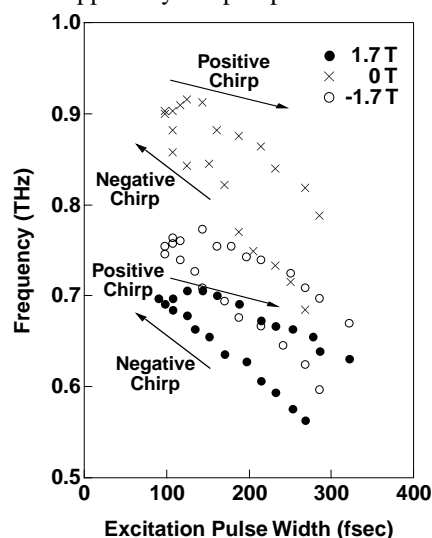


Figure 1. Center frequency spectrum dependence of THz radiation with different excitation chirp, pulse duration and magnetic field. Close circle, open circle and cross show 1.7 T, -1.7 T and 0 T, respectively.

VIII-A-5 LiCAF Crystal as a New Vacuum Ultraviolet Optical Material with Transmission Down to 112 nm

KOZEKI, Toshimasa; SAKAI, Masahiro; LIU, Zhenlin; OHTAKE, Hideyuki; SARUKURA, Nobuhiko; SEGAWA, Yusaburo¹; OBA, Tomoru²; SHIMAMURA, Kiyoshi³; BALDOCHI, Sonia L.³; NAKANO, Kenji³; MUJILATU, Na³; FUKUDA, Tsuguo³

(¹RIKEN; ²Optron Inc.; ³Tohoku Univ.)

LiCaAlF₆ (LiCAF) was found to be an ideal optical material for the vacuum ultraviolet region due to its superior transmission characteristic of down to 112 nm, its non hygroscopic nature, and its better mechanical properties compared with LiF.

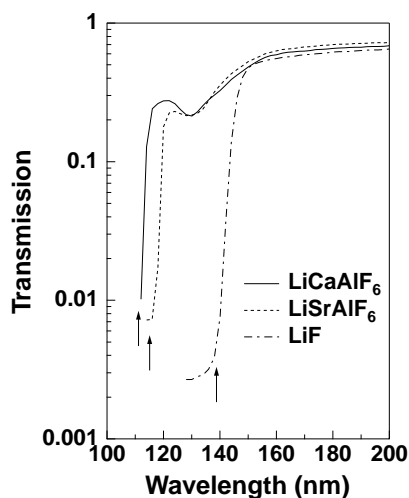


Figure 1. Transmission characteristics of LiCAF, LiSAF, LiF.

VIII-A-6 High Average Power Mode Locked Ti:Sapphire Laser with Intracavity Continuous-Wave Amplifier and Strained Saturable Bragg Reflector

LIU, Tze-An; HUANG, Kai-Fung; PAN, Ci-Ling; LIU, Zhenlin; OHTAKE, Hideyuki; SARUKURA, Nobuhiko

We demonstrate a new scheme for the generation of high average power femtosecond pulses by incorporating an intracavity amplifier and a strained saturable Bragg reflector with low saturation fluence for self-starting mode locking. When the Ti:sapphire oscillator and intracavity amplifier are pumped at 10 W and 15 W, respectively, the average output power is as high as 1.62 W. The pulse duration is about 145 fs, and the peak power reaches 160 kW at a 68 MHz repetition rate. The pulse-formation time of 400 μ s is sufficiently short to sustain stable mode locking.

VIII-A-7 THz Radiation from Intracavity Saturable Bragg Reflector in Magnetic Field with Self-Started Mode-Locking by Strained Saturable Bragg Reflector

LIU, Tze-An; HUANG, Kai-Fung; PAN, Ci-Ling; LIU, Zhenlin; ONO, Shingo; OHTAKE, Hideyuki; SARUKURA, Nobuhiko

We demonstrate a new configuration for intracavity generation of THz radiation. A magnetic-field-biased saturable Bragg reflector (SBR) located inside the femtosecond laser cavity is the emitter, while a strained saturable Bragg reflector (SSBR) achieves self-started mode-locking without focusing. The calibrated power of the emitted THz radiation is estimated to be approximately 45 nW with a peak frequency at 0.72 THz and width of approximately 0.7 THz under a 0.88 T magnetic field. The quadratic dependence of THz-radiation power by the SBR on the magnetic field is also observed for the first time.

VIII-A-8 High-Gain, Reflection-Double Pass, Ti:Sapphire Continuous-Wave Amplifier Delivering 5.77 W Average Power, 82 MHz Repetition Rate, Femtosecond Pulses

LIU, Zhenlin; MURAKAMI, Hidetoshi; KOZEKI, Toshimasa; OHTAKE, Hideyuki; SARUKURA, Nobuhiko

A confocal, reflection-double-pass, Ti:sapphire continuous-wave ~cw! amplifier with a small signal gain of 4.2 has been invented. Femtosecond pulses with an 82 MHz repetition rate from a mode-locked Ti:sapphire laser are amplified to 5.77 W average power with a slightly saturated gain of 3.7 through an amplifier pumped by three cw green lasers, and the extraction efficiency reaches 10.6%.

VIII-B Development and Research of Advanced Tunable Solid State Lasers

Diode-pumped solid-state lasers can provide excellent spatial mode quality and narrow linewidths. The high spectral power brightness of these lasers has allowed high efficiency frequency extension by nonlinear frequency conversion. Moreover, the availability of new and improved nonlinear optical crystals makes these techniques more practical. Additionally, quasi phase matching (QPM) is a new technique instead of conventional birefringent phase matching for compensating phase velocity dispersion in frequency conversion. These kinds of advanced tunable solid-state light sources, so to speak "Chroma Chip Lasers," will assist the research of molecular science.

In this projects we are developing Chroma Chip Lasers based on diode-pumped-microchip-solid-state lasers and advanced nonlinear frequency conversion technique.

VIII-B-1 Performance of Widely Tunable Yb:YAG Microchip Lasers

SAIKAWA, Jiro; KURIMURA, Sunao; PAVEL, Nicolaie; SHOJI, Ichiro; TAIRA, Takunori

[OSA TOPS on ASSL 2000 34, 106 (2000)]

The properties of the trivalent ytterbium ion doped YAG, such as a smaller quantum defect, longer upper state lifetime, simple energy structure (no excited state absorption) and so on, would promise to achieve a high power and high stability laser operation in microchip configurations. In addition, the wide emission bandwidth of the material around 1 μm allows tunable and/or mode-locked operation. In this work, we have developed a tunable intracavity frequency-doubled Yb:YAG microchip laser that outputs a maximum green power of 520mW with single frequency around the Ar^{3+} laser wavelength of 515 nm by using a 400- μm thick Yb:YAG. By using LBO crystal a wide tuning range from 515.3 to 537.7 nm ($\Delta\lambda = 22.4$ nm, $\Delta\nu = 24.4$ THz) was obtained (Figure 1). Then, we applied this tunable green laser to a wavelength-multiplexing holographic memory. We recorded 3 discrete images at 3 different wavelengths in the same position of a 600 ppm Fe-doped LiNbO_3 crystal and each image was reconstructed at each wavelength. The laser was proven to have a narrow linewidth and a wide tunability, in order to satisfy wavelength-multiplexing in the holographic storage system as shown in Figure 2. Next, in order to evaluate the potential of Yb:YAG tunability, the wide-bandwidth reflectivity dielectric mirror was deposited directly onto the Yb:YAG microchip. The output coupling mirror had a radius of curvature of 30 mm, and the cavity length was 25 mm. Experimental result of the tunability of the Yb:YAG microchip laser for different output couplers. With a reflectivity of 99.9% around 1010~1100 nm, the widest tunability of 84.5 nm, from 1024.1 to 1108.6 nm was obtained. The output beam was coupled as partially reflected beam at the birefringent filter. The oscillation range that extends beyond the Yb:YAG gain bandwidth, 9.5 nm, was realized since it has a simple energy-level manifolds. If it possible to keep wide band ($\Delta\nu \sim 22.4$ THz) laser oscillation under mode-locking operation, transform-limited pulsewidth of approximately 50 fs should be feasible. The tuning bandwidth increased by using the high-reflectivity output coupler and peak wavelength shifted to longer wavelength. The shorter band-edge was limited by increase of reabsorption loss in the

Yb:YAG, and longer band-edge by coating bandwidth in our experiment. The bandwidth of 22.4 THz indicates the potential of mode-locked operation of the Yb:YAG laser.

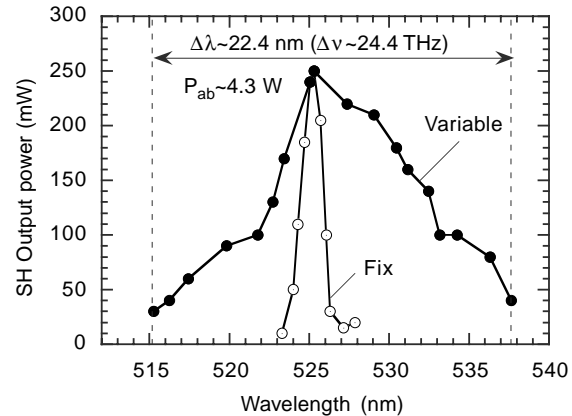


Figure 1. Tuning curve of the intracavity frequency-doubled Yb:YAG microchip laser.

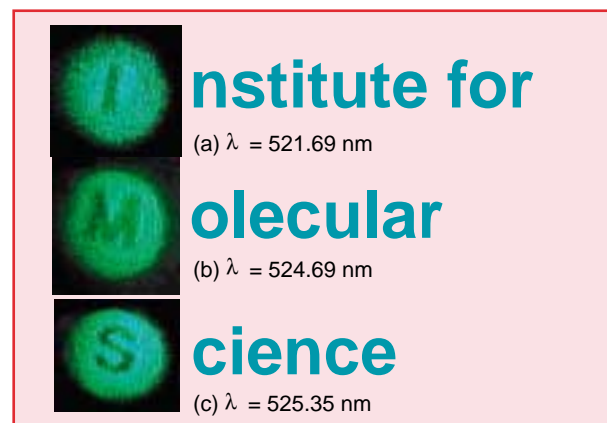


Figure 2. Reconstructed images from wavelength-multiplexed holograms by the tunable intracavity frequency-doubled Yb:YAG laser.

VIII-B-2 High Average Power Diode-Pumped Composite Nd:YAG Laser with Cr^{4+} :YAG Saturable Absorber for Passive Q-Switching

PAVEL, Nicolaie; KURIMURA, Sunao; SHOJI, Ichiro; SAIKAWA, Jiro; TAIRA, Takunori

[CLEO/Europe CWB 0006 (2000)]

Passive Q-switching technique is attractive for

scientific and industrial applications that do not require accurate repetition rates. This technique can significantly simplify the operation, improve the efficiency, the reliability and the compactness, and reduce the laser costs. In a composite rod both the peak temperature rise and the thermal stress induced by optical pumping are reduced compared to a nonbonded crystal. In this work we show that these improvements, which reduce the thermal lensing effect, made a composite medium a good solution for improving output performances of high average power passively Q-switched lasers.

In experiments we used a composite Nd:YAG rod fabricated by diffusion bonding of a Nd:YAG (5-mm length, 1.1-at.% Nd doping) to an undoped YAG piece (1-mm length). The medium was end-pumped by a 1.55-mm diameter, 0.11-NA OPC fiber-bundles diode. With a plane-plane resonator of 80-mm length and an output mirror of 95% reflectivity at 1064nm, this configuration delivers a cw maximum output power of 7.7 W with an optical efficiency of 36.9%. The slope efficiency is 39.4%, and the laser beam M^2 factor varies among 1.1 and 2.3 on the pump power range. With a Nd:YAG medium (10-mm length, 1.3-at.% Nd doping), the maximum cw power was 8.2-W at 21.8-W absorbed power, the slope efficiency was 41.6%, and the laser beam M^2 factor varies between 1.2 and 3.3 on the pump power range. Cr^{4+} :YAG crystals with varying low-signal transmission T_0 have been used, as well as resonators of various length and output couplings. As an example, Figure 1 shows the average output power for the composite medium and Cr:YAG absorbers of $T_0 = 89\%$, 85% , and 80% . A plane-plane resonator of 80-mm length with an $R = 90\%$ output coupler was considered. A maximum average power of 4.21-W in a laser beam of $M^2 = 1.3$ resulted for the Cr:YAG absorber of $T_0 = 89\%$. The laser generated pulses of 48-ns duration at 24-kHz (~ 3.65 kW peak power). With the Nd:YAG medium a maximum average power of 3.9-W in a beam of $M^2 = 1.9$ resulted. When the resonator length was of 40-mm and a Cr:YAG crystal of $T_0 = 80\%$ was used, the composite Nd:YAG laser outputs a maximum average power of 2.6-W in a beam of $M^2 = 1.45$. The pulse width was 17.5-ns, the pulse energy is 0.285-mJ, and the peak power is 16.3-kW. Using the Nd:YAG medium, the maximum average power and beam M^2 factor decreases to 1.8-W and 1.9, respectively. Shorter resonators in spite of reducing the average output power will increase the Q-switched pulse peak power. This way a simple and compact-pumping source for parametric conversion into mid-IR region could be obtained.

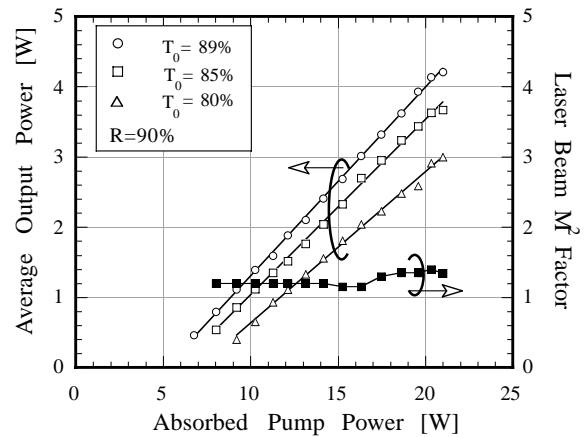


Figure 1. Average output power and beam M^2 factor as a function of absorbed pump power for the composite Nd:YAG, Cr:YAG absorbers.

VIII-B-3 Optical Properties and Laser Characteristics of Highly Nd^{3+} -Doped $\text{Y}_3\text{Al}_5\text{O}_{12}$ Ceramics

SHOJI, Ichiro; KURIMURA, Sunao; SATO, Yoichi; TAIRA, Takunori; IKESUE, Akio¹; YOSHIDA, Kunio²
(¹JFCC; ²Osaka Inst. Tech.)

[*Appl. Phys. Lett.* **77**, 939 (2000)]

Diode-pumped microchip solid-state lasers have such advantages as compactness, high efficiency, high power, and low numbers of longitudinal and transverse modes. A wide variety of materials have been investigated to develop more efficient and higher power microchip lasers. Although Nd:YVO₄ is a suitable material for highly efficient microchip laser owing to its large absorption cross section, high power operation is difficult because its thermo-mechanical properties are poor. On the other hand, while Nd:YAG has good thermal properties, highly efficient microchip laser has never been reported since high doping (> 1 at. %) of neodymium into the YAG crystal is impossible, limiting pump absorption. Recently developed transparent Nd:YAG ceramics are attractive materials because high doping of neodymium is possible without degrading the thermal conductivity. In this work we report measurements of the absorption spectra and the fluorescence lifetime of ceramic Nd:YAG in order to show that it is a promising material as a highly efficient and high power microchip laser. Moreover, we characterized its laser performance. Figure 1 shows the absorption spectra of 2.2 and 4.8 at. % Nd:YAG ceramics and 1.1 at. % single crystal. The 4.8 at. % Nd:YAG ceramic has an absorption coefficient (30.4 cm^{-1}) as large as that of Nd:YVO₄.

The input-output power characteristics of 2.4 and 4.8 at. % ceramics and a 0.9 at. % single crystal with microchip structures (the thickness of laser medium < 1mm) are shown in Figure 2. For the 4.8 at. % ceramic, 2.3 times higher output was achieved than that for the single crystal, which indicates the advantage of Nd:YAG ceramics as highly efficient miniature or microchip lasers. We estimated the round-trip cavity

losses by obtaining the slope efficiencies with different output-couplers. From this, we found that the loss of the 2.4 at. % ceramic is as low as that of the single crystal. It is concluded that highly Nd³⁺-doped YAG ceramics are promising as a highly efficient, high-power microchip laser material.

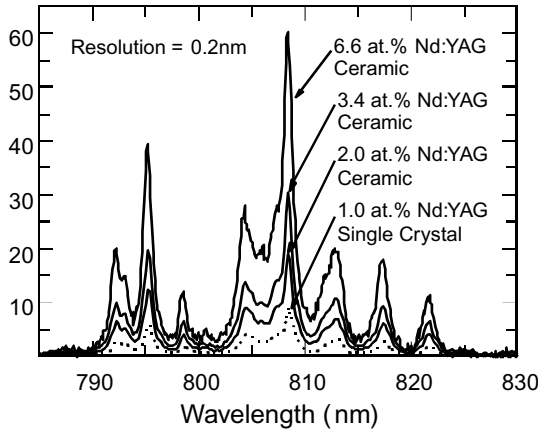


Figure 1. Absorption spectra of Nd:YAG ceramics (solid curves) and Nd:YAG single crystal (dashed curve).

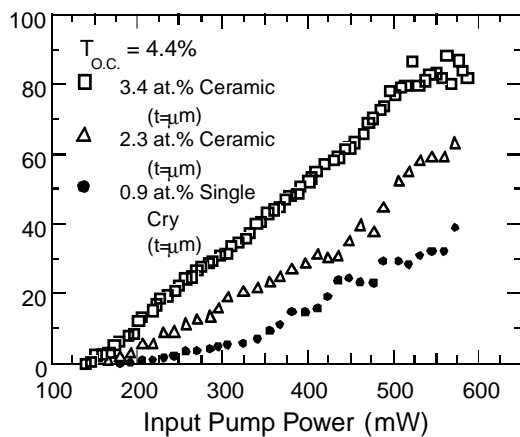


Figure 2. Dependence of the output power on the input pump power for the Nd:YAG ceramics and the single crystal.

VIII-B-4 Development of Multifunction Nonlinear Optical Wavelength Converter

KURIMURA, Sunao; PAVEL, Nicolaie; SHOJI, Ichiro; TAIRA, Takunori

[Autumn Meeting of Japan Applied Physics Society 3a-Q-22 (2000)]

Wavelength conversion based on nonlinear optics yields high efficiency without any sacrifice in coherency. Recently developed *Quasi-Phase Matching (QPM)* technique has produced designability of phase matching wavelength and efficiency, together with artificial characteristics of converters in space, frequency, and time domains by using digital patterns defined by photolithography. QPM giving new degree of freedom thus brought about stronger impact than growth of new crystals in the nonlinear optics. We here proposed efficient wide-band infrared generation with cascaded QPM crystals for optical parametric oscillation

(OPO) and difference frequency generation (DFG) around 6 μm region, where double bond structures of molecules have characteristic absorption lines. Figure 1 illustrates the geometry, measured emission wavelengths in OPO and required QPM period in DFG in efficient nonlinear crystal, lithium niobate (LN). Since LN has moderate absorption at 6 μm , direct access to 6 μm induces thermal fluctuation enhanced in OPO cavity. Our approach is to use OPO in the transparent region of LN and access to 6 μm by single-pass DFG, which is less sensitive to thermal disturbance. We devised first OPO stage and obtained IR emission plotted in Figure 1(b) with closed circles. The 0.5mm-thick QPM device with a period of 30.9 μm was fabricated by electric field poling in liquid electrodes as shown in Figure 1(d).

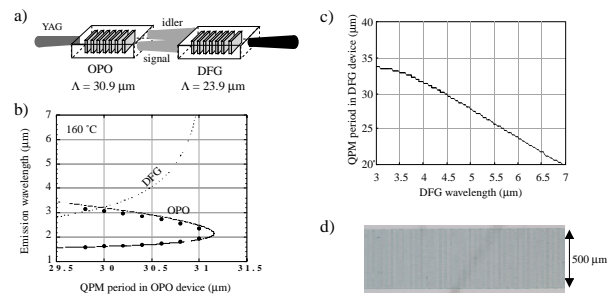


Figure 1. QPM OPO-DFG light source for widely tunable IR light: a) geometry, b) wavelength tunability depending on QPM period, c) calculated DFG period, d) periodical domains in a QPM LN device.

VIII-B-5 Periodical Twinning in Crystal Quartz for Ultraviolet Nonlinear Optics

KURIMURA, Sunao; FEJER, Martin¹; SHOJI, Ichiro; TAIRA, Takunori; UESU, Yoshiaki²; NAKAJIMA, Hirochika²
(¹Stanford Univ., U. S. A.; ²Waseda Univ.)

[*Oyobuturi* **69**, 548 (2000)]

Crystal quartz is attractive for operation in ultraviolet nonlinear optics, which has low absorption from 150 nm, high chemical stability, and low thermo-optic coefficients compared with conventional ultraviolet nonlinear crystals. Growth techniques are well established because of widespread in surface-acoustic-wave and timing applications, but unfortunately, it doesn't meet the birefringent phase matching condition due to small birefringence, and electric field poling condition due to lack of ferroelectricity. We devised a new poling technique in crystal quartz using mechanical twinning and demonstrated periodical polarity reversal by using thermal stress. Figure 1 shows an observed twin structure with a period of 80 μm , obtained by thermally induced stress between patterned Cr films and a quartz. The Cr patterned substrate was heated to just below Curie temperature in order to attain reasonable film stress and reduce coercive stress. Twins tend to generate from the edge of Cr pattern and the required duty ratio of Cr to the period was more than 0.5. The depth of twins, however, were several microns, indicating not

suitable for bulk nonlinear optics. New technique is under development to improve the depth profile of the twins for a practical UV generator.

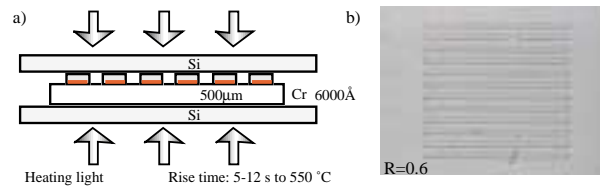


Figure 1. Twin patterning in crystal quartz: a) patterning method by the thermally induced in-plane stress, b) observed periodical twins with a period of 80 μm period, R : duty ratio of the Cr film to the period.

Research Center for Molecular Materials

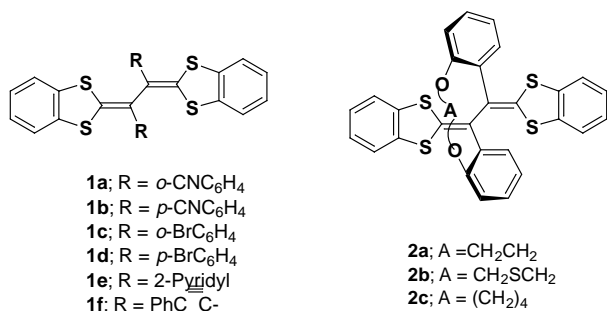
VIII-C Development of Novel Heterocyclic Compounds and Their Molecular Assemblies for Advanced Materials

Heterocycles containing sulfur and/or nitrogen atoms are useful as components of functional materials since heteroatoms in their rings are helpful to stabilize ions or ion-radical species, and extended π -conjugation decreases Coulombic repulsion. In addition intermolecular interactions caused by heteroatom contacts can be expected to form novel molecular assemblies. In this project new electron acceptors, donors, and donor-acceptor compounds based on heterocycles such as 1,2,5-thiadiazole and 1,3-dithiole were synthesized and their properties including those of the charge-transfer complexes or ion-radical salts were investigated. Unique crystal structures were constructed by using weak intermolecular interactions such as hydrogen bonding or heteroatom contacts. Heterocyclic oligomers with rigid structures were also synthesized for molecular wires.

VIII-C-1 Preparation of New TTF Vinylogues Containing Substituents at the Vinyl Positions

YAMASHITA, Yoshiro; TOMURA, Masaaki

TTF vinylogues **1** have a stronger electron-donating ability and reduced on-site Coulomb repulsion owing to the extended π -delocalized system. The physical properties and structures can be tuned by the substituents at the vinyl positions. For example the ortho-substituted phenyl groups can keep the TTF vinylogue skeleton plane by taking twisting conformations, leading to the stable cation radical states.¹⁾ We have now prepared the new derivatives **1** and **2**, and investigated their properties. New compounds **1a–d** possess cyano or bromo substituents which can induce intermolecular interactions. The synthesis is based on oxidative coupling reaction of the corresponding 1,4-dithiafulvenes. **1e** with 2-pyridyl substituents and **1f** with phenylethynyl groups were also synthesized. **1f** has no steric hindrance caused by substituents. Furthermore, we have obtained cyclophane-type molecules **2** which have a bridge between the phenyl substituents. The following oxidation potentials of new molecules were observed. **1a**; 0.61, 0.84, **1b**; 0.64 (2e), **1c**; 0.51, 0.75, **1d**; 0.68 (2e), **1e**; 0.91 (irrev.), **1f**; 0.57, 0.76, **2a**; 0.48, 0.64, **2b**; 0.52, 0.65; **2c**; 0.40, 0.63V vs. SCE.



Reference

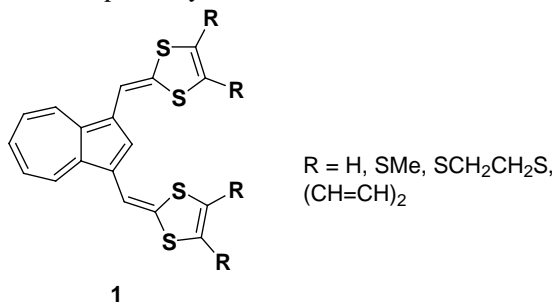
1) Y. Yamashita, M. Tomura, M. B. Zaman and K. Imaeda, *Chem. Commun.* 1657 (1998).

VIII-C-2 Preparation, Structure, and Properties of 1,3-Bis(1,4-dithiafulven-6-yl)azulenes

OHTA, Akira¹; YAMAGUCHI, Kyoko¹;

FUJISAWA, Naoki¹; YAMASHITA, Yoshiro;
FUJIMORI, Kunihide¹
(¹Shinshu Univ.)

Novel bis(1,3-dithiole) electron donors **1** containing an azulene spacer unit were prepared from 1,3-diformylazulene using a Wittig-Horner reaction in 20–85% yields. The first oxidation potentials of **1** are lower than that of TTF, indicating that they are stronger donors than TTF as predicted by the PM3 calculations. In addition to the oxidation waves, they show an irreversible reduction peak at *ca.* –1.4 V. This amphoteric nature is consistent with the absorption data where the longest absorption maxima are observed at 733–762 nm in dichloromethane. The structure features of a benzo-fused derivative were investigated by X-ray analysis. One of the 1,4-dithiafulvenyl groups and the azulene moiety are in almost coplanar, while the other one twists with a torsion angle of 20.8°. The spectroelectrochemical studies on the methylthio derivative reveals that the cation radical and dication state have the longest absorption maxima at 612 and 721 nm, respectively.

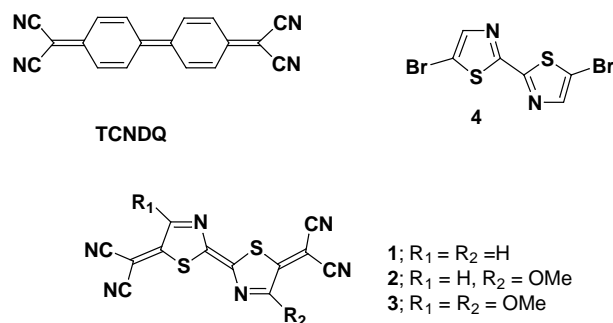


VIII-C-3 Synthesis and Characterization of Novel Strong Electron Acceptors: Bithiazole Analogues of Tetracyanodiphenoquinodimethane (TCNDQ)

SUZUKI, Kazuharu; TOMURA, Masaaki;
TANAKA, Shoji; YAMASHITA, Yoshiro

Pyridine analogues of TCNQ are unstable due to the much stronger electron accepting ability. On the other hand, thiophene-TCNQs are generally weak electron acceptors due to the electron donating effect of the thiophene ring. Therefore, we have designed a new

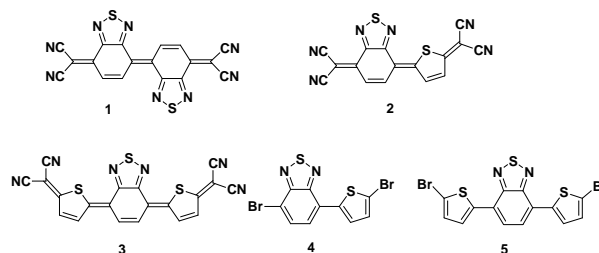
electron acceptor **1**, a TCNDQ analogue containing Nitrogen and Sulfur atoms in the skeleton. **1** was prepared by using Pd-catalyzed coupling reaction of dicyanomethanide to a dibromo precursor **4**. The new acceptor shows a strong electron accepting ability and small on-site Coulomb repulsion. The methoxy derivatives **2** and **3** were also obtained by substitution reaction of **1** with methanol. The reduction potentials of **2** and **3** are lower than that of **1** due to the electron donating methoxy substituents. The X-ray analysis of **1** and **2** has revealed the planar structures containing a double bond with *E*-configuration. The acceptors **1**–**3** have characteristic strong absorptions around 550 nm. **1** afforded several charge transfer complexes with electron donors such as TTF.



VIII-C-4 Heterocyclic TCNQ Analogues Containing Thiophene and Benzothiadiazole Units

SUZUKI, Kazuharu; TOMURA, Masaaki; YAMASHITA, Yoshiro

Sulfur containing TCNQ analogues are highly polarized and are expected to have strong intermolecular interactions by heteroatom contacts. We have recently prepared a TCNDQ derivative **1** containing fused thiadiazole rings. As an extension of this work, we have now prepared new π -extended electron acceptors **2** and **3** composed of benzothiadiazole and thiophene units. They were synthesized using the Pd catalyzed reaction of the corresponding dibromides **4** and **5** with malononitrile anion. The absorption maxima of **2** and **3** were observed at 524 and 635 nm in dichloromethane, respectively. **2** shows stepwise one-electron reduction waves at +0.07 and -0.17 V vs. SCE, while **3** shows a one-step two-electron reduction wave at +0.08 V vs. SCE. The values of the first reduction potentials are lower than that of TCNQ, indicating that they are not so strong acceptors. However, they are still stronger acceptors than the corresponding thiophene-TCNQ analogues. The X-ray analysis revealed that **2** has a planar geometry and the central double bond takes a *Z*-configuration. **2** gave various charge transfer complexes and anion radical salts. The Me_4P^+ salt exhibits a high conductivity of 8.4 Scm^{-1} .



VIII-C-5 Crystal Engineering in π -Overlapping Stacks: Unusual One- and/or Two-Dimensional Stacking of π -System in the Crystal Structure of the Cation Radical Salts of Tetrathiafulvalene Vinyllogues

TOMURA, Masaaki; YAMASHITA, Yoshiro

[*CrystEngComm* 14 (2000)]

One- and/or two-dimensional π -overlapping stacks have been found in the crystals of the cation radical salts of the tetrathiafulvalene vinyllogues **1** and **2** having *o*-substituted phenyl groups at the vinyl positions. The packing mode in the two-dimensional π -stacks could be modified depending on the counter anions. We have observed the pseudo two-dimensional stacking and the zigzag two-dimensional stacking with an angle of nearly 90° in the crystal structure of **1**- $FeCl_4$ and **1**- ReO_4 salts, respectively. In the case of **2**- PF_6 - $(H_2O)_8$ salt, we have observed not the two-dimensional π - π overlapping stack found in the cation radical salts of **1**, but the one-dimensional stacking of π -system. The one-dimensional overlapping mode of **2** has brought a square grid-like structure (Figure 1) with a void in which eight water molecules are occupied. The 1,3-dithiole rings in **2** are unfavorable for π - π intermolecular interactions due to the less π -delocalization and steric interactions of the ethylenedithio parts compared to those in **1**. This seems to lead to the novel one-dimensional structure, not the two-dimensional one.

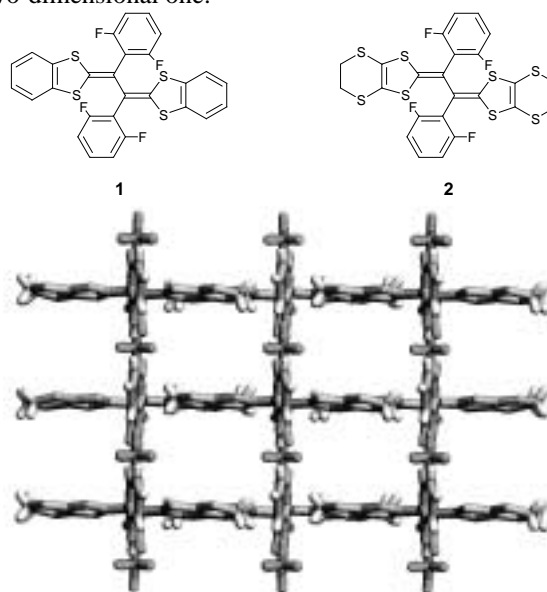


Figure 1. Crystal structure of **2**- PF_6 - $(H_2O)_8$ salt viewed along the *c* axis. The water molecules are omitted for clarity.

VIII-C-6 One-Dimensional Supramolecular Tapes in the Co-Crystals of 2,5-Dibromo-3,6-dihydroxy-1,4-benzoquinone (Bromanilic Acid) with Heterocyclic Compounds Containing a Pyrazine Ring Unit

TOMURA, Masaaki; YAMASHITA, Yoshiro

[*CrystEngComm* 16 (2000)]

The design of new molecular architectures for crystal engineering has generated great interest in recent years. We have carried out co-crystallization of 2,5-dibromo-3,6-dihydroxy-1,4-benzoquinone (bromanilic acid) with heterocyclic aromatic compounds, phenazine, quinoxaline and pyrazine. The X-ray crystallographic analyses of the co-crystals suggest the supramolecular synthon formed with bromanilic acid and the heterocyclic compounds can yield the robust one-dimensional supramolecular tapes (Figure 1) and realize preserved interesting crystal structures.

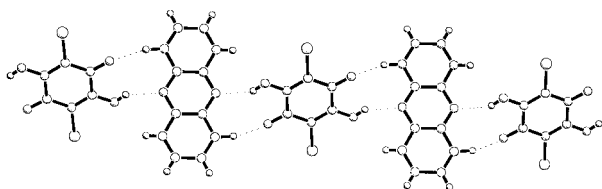


Figure 1. One-dimensional tape in the co-crystal of bromanilic acid with phenazine.

VIII-C-7 A Decamethylferrocene [Fe(C₅Me₅)₂] and Chloranilic Acid (CA) Complex with Hydrogen Bonded Supramolecular Structure between CA and H₂O

ZAMAN, Md. Badruz; TOMURA, Masaaki; YAMASHITA, Yoshiro; SAYADUZZAMAN, Md.¹; CHOWDHURY, A. M. Sarwaruddin¹
(¹Dhaka Univ.)

[*CrystEngComm* 9 (1999)]

The chloranilic acid as acceptor (A) has been used to prepare crystalline materials with organometallic decamethylferrocene as donor (D). The structure was obtained by single crystal X-ray analysis and the stoichiometric ratio [D:A:H₂O = 1:1:1] was confirmed by elemental analysis. These analyses reveal the molecular complex as [Fe(C₅Me₅)₂]⁺[CA]⁻[H₂O]. The water molecules in this crystal act as cohesive elements by connecting the anions through O–H...O hydrogen bonds to form an infinite one-dimensional supramolecular structure along the b axis (Figure 1). This solid-state structural aspects of DA solids has interesting, highly charged ground states, which are not commonly observed in Fe(C₅Me₅)₂ complexes due to the paucity of stability and highly charged species.



Figure 1. View of the hydrogen bonded network with CA and H₂O molecule.

VIII-C-8 New Hydrogen Bond Donor-Acceptor Pairs between Dipyriddylacetylenes and 2,5-Dichloro-3,6-dihydroxy-1,4-benzoquinone

ZAMAN, Md. Badruz; TOMURA, Masaaki; YAMASHITA, Yoshiro

[*Org. Lett.* 2, 273 (2000)]

The crystalline donor-acceptor hydrogen bonding complexes between 2,5-chloro-3,6-dihydroxy-1,4-benzoquinone (chloranilic acid, H₂CA) and dipyriddylacetylenes (DPA) [2,2'-DPA, 3,3'-DPA and 4,4'-DPA] were prepared and crystal structures were revealed by X-ray analysis. The structures of the complexes are formed by intermolecular hydrogen bonding interactions and demonstrate three beautiful supramolecular architectures based on a new common supramolecular synthon (Figure 1), which allows controlling the crystal structures, ionicity and stacking arrangements.

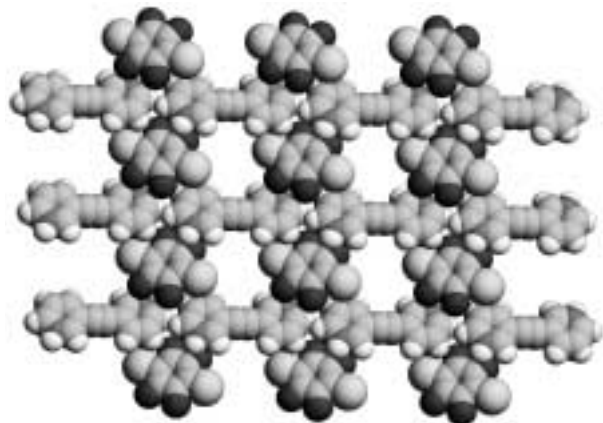


Figure 1. Square grids structure of [CA]²⁻[3,3'-H₂DPA]²⁺·(H₂O)_{3,3} complex. The water molecules are omitted for clarity.

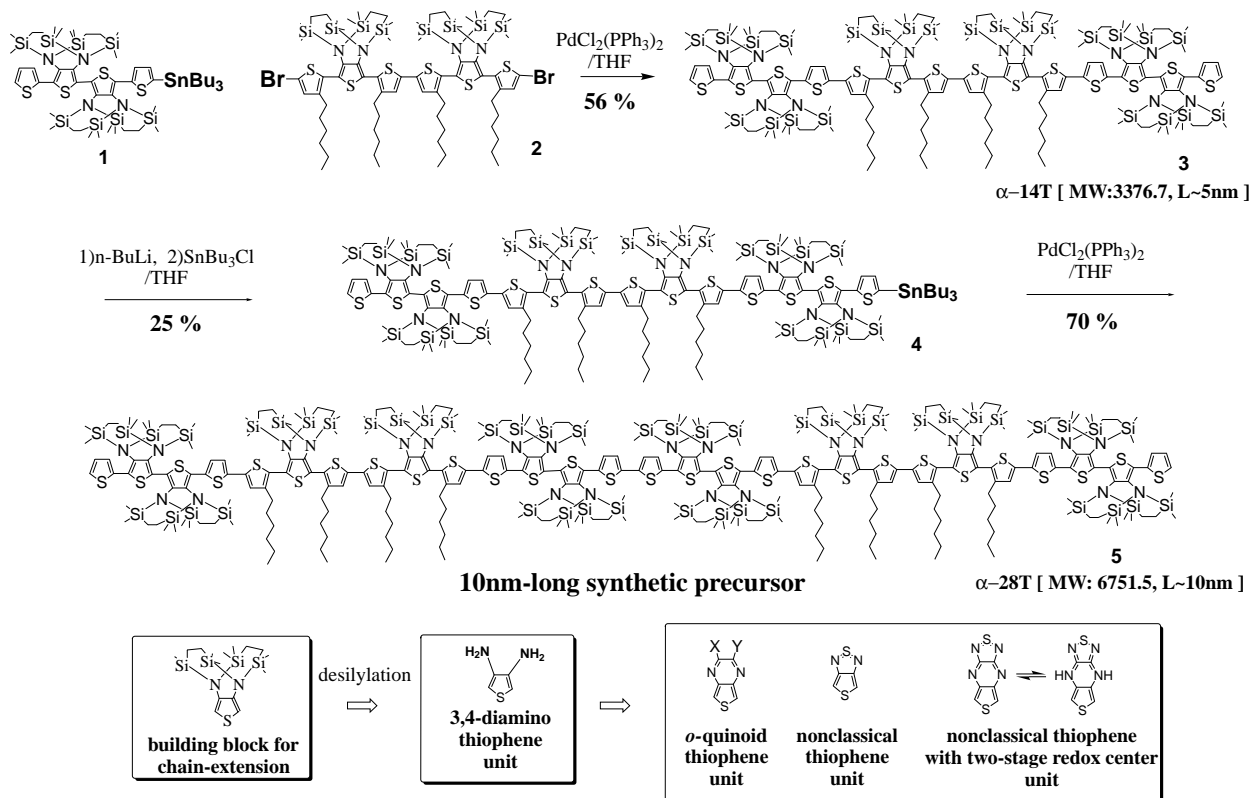
VIII-C-9 Novel Synthetic Approach to 5–10 nm Long Functionalized Oligothiophenes

TANAKA, Shoji ; YAMASHITA, Yoshiro

The development of precisely-defined oligomers with extended π -conjugation length comparable to the inter-electrode gap currently made by nano-patterning techniques (5–10 nm gap) has generated a great deal of interest. The reason for this is that highly oligomers of this class will become an important tool for providing specific information on the parameters controlling the long-distance electron-tunneling through a single molecular wire. Here we will report a new synthetic approach to a series of precisely defined 5–10 nm long oligothiophenes, using N-silyl-protected 3,4-

diaminothiophene as a key building unit. Scheme 1 shows the synthetic pathways for α -14T (**3**: $l \sim 5$ nm) and α -28T (**5**: $l \sim 10$ nm) derivatives. Purification of all oligomers (**1–5**) was achieved by preparative gel permeation chromatography, and the purity was clearly revealed by MALDI-TOF mass spectrometry in the

positive ion and linear detection mode using dithranol as matrix. The desilylation and further chemical modifications of the N-silyl-protected 3,4-diaminothiophene moieties of the obtained oligomers will afford various types of 5–10 nm long functionalized oligomers.



Scheme 1.

VIII-D Electronic Structures and Reactivities of Active Sites of Metalloproteins

Metalloproteins are a class of biologically important macromolecules which have various functions such as oxygen transport, electron transfer, oxidation, and oxygenation. These diverse functions of metalloproteins have been thought to depend on the ligands from amino acid, coordination structures, and protein structures in immediate vicinity of metal ions. In this project, we are studying the relationship between the structures of the metal active sites and functions of metalloproteins.

VIII-D-1 Resonance Raman Spectra of Legitimate Models for the Ubiquitous Compound I Intermediates of Oxidative heme Enzymes

CZARNECKI, Kazimierz¹; KINCAID, James R.¹; FUJII, Hiroshi
(¹Marquette Univ.)

[*J. Am. Chem. Soc.* **121**, 7953 (1999)]

Resonance Raman (RR) spectra are reported for two models of the compound I intermediates of oxidative heme proteins; namely, the imidazole (Im) and 2-methyl-imidazole (2-MeIm) complexes of the ferryl π -cation radical derivative of iron-(5,10,15,20-tetramesitylporphyrin), $[\text{O}=\text{Fe}(\text{TMP}^+)(\text{Im})]^+$ and $[\text{O}=\text{Fe}(\text{TMP}^+)]^+$, which are stabilized in dichloromethane solution at -80°C . The present study yields high quality RR spectra of these complexes and provides the first opportunity to compare the $\nu(\text{Fe}=\text{O})$ stretching modes and the structure-sensitive core maker modes for a ferrylporphyrin π -cation radical with the corresponding modes of the neutral parent bearing the same trans-axial ligand. While the observed shifts in the frequencies of the core modes are in agreement with those expected upon formation of the π -cation radical, the results suggest that the isolated effect of macrocycle oxidation on the $\text{Fe}=\text{O}$ stretching frequency is rather small; the observed shift being only about 4 cm^{-1} to lower frequency.

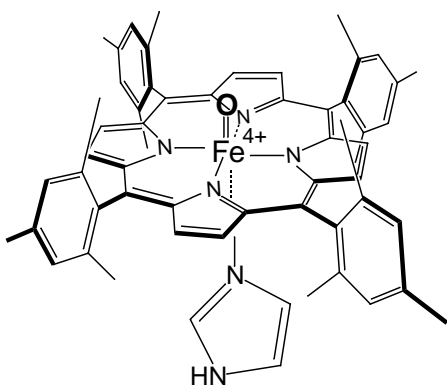


Figure 1. Structure of model complexes of the compounds I of oxidative heme proteins.

VIII-D-2 Spin Distribution in Low-Spin (meso-Tetraalkylporphyrinato)iron(III) Complexes with $(dxz,dyz)^4(dxz)^1$ Configuration. Studies by ¹H-NMR, ¹³C-NMR, and EPR Spectroscopies

IKEUE, Takahisa¹; OHGO, Yoshiki¹; SAITOH,

Takashi¹; NAKAMURA, Mikio¹; FUJII, Hiroshi;
YOKOYAMA, Masataka²
(¹Toho Univ. Sch. Med.; ²Chiba Univ.)

[*J. Am. Chem. Soc.* **122**, 4068 (2000)]

¹H-NMR, ¹³C-NMR, and EPR studies of a series of low-spin (meso-tetraalkylporphyrinato)iron(III) complexes, $[\text{Fe}(\text{TRP})(\text{L})_2]\text{X}$ where R = n-Pr, c-Pr, and i-Pr and L represents axial ligands such as imidazoles, pyridines, and cyanide, have revealed that the ground-state electron configuration of $[\text{Fe}(\text{TnPrP})(\text{L})_2]\text{X}$ and $[\text{Fe}(\text{TcPrP})(\text{L})_2]\text{X}$ is presented either as the common $(dxz,dyz)^2(dxz,dyz)^3$ or as the less common $(dxz,dyz)^4(dxz)^1$ depending on the axial ligands. The ground-state electron configuration of the isopropyl complexes $[\text{Fe}(\text{TiPrP})(\text{L})_2]\text{X}$ is, however, presented as $(dxz,dyz)^4(dxz)^1$ regardless of the kind of axial ligands. In every case, the contribution of the $(dxz,dyz)^4(dxz)^1$ state to the electronic ground state increases in the following order: HIm < 4-Me₂NPpy < 2-MeIm < CN⁻ < 3-MePy < Py < 4-CNPy. Combined analysis of the ¹³C and ¹H NMR isotropic shifts together with the EPR *g* values have yielded the spin densities at the porphyrin carbon and nitrogen atoms. Estimated spin densities in $[\text{Fe}(\text{TiPrP})(4\text{-CNPy})_2]^+$, which has the purest $(dxz,dyz)^4(dxz)^1$ ground state among the complexes examined in this study, are as follows: meso-carbon, +0.045; β -pyrrole carbon, +0.0088; α -pyrrole carbon, -0.00026; and pyrrole nitrogen, +0.057. Thus, the relatively large spin densities are on the pyrrole nitrogen and meso-carbon atoms. The result is in sharp contrast to the spin distribution in the $(dxz,dyz)^2(dxz,dyz)^3$ type complexes; the largest spin density is at the α -pyrrole carbon atoms in bis(1-methylimidazole)(meso-tetraphenylporphyrinato)iron(III), $[\text{Fe}(\text{TPP})(1\text{-MeIm})_2]^+$, as determined by Goff. The large downfield shift of the meso-carbon signal, $\delta +917.5\text{ ppm}$ at -50°C in $[\text{Fe}(\text{TiPrP})(4\text{-CNPy})_2]^+$, is ascribed to the large spin densities at these carbon atoms. In contrast, the large upfield shift of the β -pyrrole carbon signal, -293.5 ppm at the same temperature, is caused by the spin polarization from the adjacent meso-carbon and pyrrole nitrogen atoms.

VIII-D-3 Post-Assembly Insertion of Metal Ions into Thiol-Derivatized Porphyrin Monolayers on gold

NISHIMURA, Noboru¹; OOI, Masanori¹; SHIMATZU, Katsuaki¹; FUJII, Hiroshi; UOSAKI, Kohei¹
(¹Hokkaido Univ.)

[*J. Electro. Chem.* **473**, 75 (1999)]

The insertion of metal ions into thiol-derivatized free base porphyrin monolayers pre-assembled on gold has been conducted by refluxing the metal ion solution in which the monolayer-coated gold electrode was immersed. The extent of the metal insertion was estimated from the decrease in the N1s peaks in X-ray photoelectron spectra (XP spectra) assigned to the pyrrole nitrogen which binds a hydrogen atoms. The insertion of Co(II) was completed by refluxing for 3 hr. Although the extent of the metal insertion for the same reflux time depends on the metal ion used, the insertion of several ions including Mn(II), Fe(II), Ni(II), Cu(II) and Zn(II) was possible. Besides XP spectra, the metal insertion was confirmed by the electrocatalytic activity of the monolayers for the reduction of molecular oxygen. The structural characterization has proved that the monolayer is stable during the reflux: neither desorption nor change in the orientation of the porphyrin molecules took place. Compared to the commonly used self-assembly of the pre-metalated porphyrin, this post-assembly metal insertion method has an advantage because neither intra nor intermolecular coordinations of the thiol functionality to the central metal ion take place, thus avoiding the unexpected disorder in the monolayer such as the formation of a multilayer, the blocking of the electrocatalytically active metal ion and loss of the anchoring functionality or thiol.

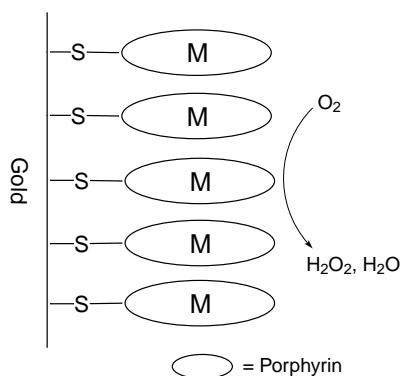


Figure 1. Porphyrin monolayer formed by the self-assembly on gold surface.

VIII-D-4 Electron Spin-Echo Envelope Modulation Spectral properties of Amidate Nitrogen Coordinated to Oxovanadium(IV) Ion

FUKUI, Koichi¹; FUJII, Hiroshi; OHYA-NISHIGUCHI, Hiroaki¹; KAMADA, Hitoshi¹
(¹*Inst. Life. Supp. Tech.*)

[*Chem. Lett.* 198 (2000)]

Increase evidence shows that vanadium plays a variety of roles in biological systems. For instance, a class of haloperoxidase requires vanadium for their enzymatic activities. Vanadium is also known to have beneficial insulin-mimetic activities, and some vanadium complexes are studied as a candidate for an orally-active anti-diabetic agent. These findings have stimulated interests in the interactions of vanadium with biological substances such as amino acids, peptides,

and proteins. In the studies on this subject, interests are often focused on carboxylate, imidazole and amino groups for vanadium-coordinating groups. However, recent studies have shown that amido group can undergo reprotonation/coordination reaction even at physiological conditions when an anchoring group is present. Therefore, it is possible that vanadium-amidate bonding actually occurs and plays some roles in biological systems. For characterization of vanadium(IV) coordination environments, electron spin-echo envelope modulation (ESEEM) spectroscopy is suited. It has been demonstrated that ESEEM results not only reveal the presence or absence of nitrogen nuclei coordinated to VO²⁺ ion (and possibly the number of the coordinating nitrogen atoms), but allow identification of equatorial nitrogens based on the empirical correlation between the type of the nitrogen and the ¹⁴N hyperfine coupling (HFC) parameter. However, neither the HFC parameters nor the nuclear quadrupole coupling (NQC) parameters are known for vanadium-coordinated amidate nitrogens. Here we report the first ESEEM results for a structurally-characterized VO²⁺-amidate complex.

VIII-D-5 Newly Designed Iron-Schiff Base Complexes as Models of Mononuclear Non-Heme Iron Active Sites

FUNAHASHI, Yasuhiro; FUJII, Hiroshi

High valent iron-oxo species have been suggested as the active intermediates for catalytic oxygenation reactions by iron-containing oxygenases. In the reaction mechanisms of heme and binuclear non-heme iron enzymes, an Fe^{IV}=O porphyrin radical species (Compound I) and a Fe^{IV}₂(μ-O)₂ species (Intermediate Q) have been found to be responsible oxidant for alkane hydroxylation and alkene epoxidation. Such the high valent iron-oxo species are inferred to involve in hydroxylation of aromatic compounds by mononuclear non-heme iron oxygenases, the reaction processes of which, however, still remains to be established. In order to gain insight into the active intermediates, we try to synthesize iron complexes with bulky schiff-base ligands as biomimetic models of mononuclear non-heme iron active sites. The active oxygen adduct of these complexes, which would be kinetically stabilized by their steric hindrance, might provide a basis for understanding the oxygenation by mononuclear iron sites.

VIII-D-6 Synthesis and Characterization of High Valent Iron Porphyrin Complexes as Models for Reaction Intermediates of Cytochrome c Oxidase

IKEUE, Takahisa; FUMOTO, Yumiko¹; ONO, Noboru¹; FUJII, Hiroshi
(¹*Ehime Univ.*)

Cytochrome c oxidase is the terminal oxidase which reduces molecular oxygen (O₂) to water (H₂O), coupling with proton pumping across the mitochondrial inner membrane. Since discovery of this enzyme, many

structural and functional studies have been done to understand its reaction mechanism. Recent X-ray analyses reveal that this enzyme contains a binuclear center, heme-a₃-Cu_B site, as a reaction site in the catalytic core, and Cu_A and Heme-a as electron transfer sites in the backbone structure, respectively. The binuclear center of the resting enzyme is ferric/cupric form. The binuclear active site is reduced to a ferrous/cuprous form by two electrons from cytochrome c through the Cu_A and heme a site. The ferrous/cuprous form of active site reacts with O₂ to yield an internal dioxygen adduct, intermediate A state, which is further converted to intermediate P and F by the aid of the electrons and protons. Although the intermediates P and

F have been studied by resonance Raman and flash-flow absorption spectroscopies, the electronic states of these intermediates are not still clear. To reveal the electronic states of these intermediates and to understand the reaction mechanism of cytochrome c oxidase, we have synthesized model complexes of the heme-a₃ site of cytochrome c oxidase. The model complex contains a formyl group at pyrrole-β position to mimic the heme a₃ and mesityl groups to stabilize high valent oxo iron species. We have succeeded in the preparation of a high valent oxo iron porphyrin complex as a model for the intermediate P by the oxidation of the ferric model complex with mCPBA or ozone.

VIII-E Molecular Mechanism of Heme Degradation and Oxygen Activation by Heme Oxygenase

Heme oxygenase (HO), an amphipathic microsomal proteins, catalyzes the regiospecific oxidative degradation of iron protoporphyrin IX (heme) to biliverdinIX α , carbon monoxide, and iron in the presence of NADPH-cytochrome P-450 reductase, which functions as an electron donor. Heme oxygenase reaction is the biosynthesis processes of bile pigments and CO which is a possible physiological messenger. Recent development in the bacterial expression of a soluble form of heme oxygenase has made it possible to prepare in the large quantities for structural studies. In this project, we are studying the molecular mechanism of heme degradation and the oxygen activation by heme oxygenase using various spectroscopic methods.

VIII-E-1 Participation of Carboxylate Amino Acid Side Chain in Regiospecific Oxidation of Heme by Heme Oxygenase

ZHOU, Hong¹; MIGITA, Taiko Catharine²; SATO, Michihiko¹; SUN, Donghu¹; ZHANG, Xuhong¹; IKEDA-SAITO, Masao²; FUJII, Hiroshi; YOSHIDA, Tadashi¹

(¹Yamagata Univ. Sch. Med.; ²Yamaguchi Univ.; ³Case West. Res. Univ. Sch. Med.)

[*J. Am. Chem. Soc.* **122**, 8311 (2000)]

The regiospecific oxidation of the α -meso position by HO is quite unique, in contrast to the non-enzymatic heme degradation that forms a mixture of four possible α , β , γ , δ -biliverdin isomers. The present study shows the first evidence of the formation of biliverdin isomers other than biliverdinIX α by HO mutants. The replacement of the highly conserved arginine 183(R183) of HO-1 with glutamic acid (E) or aspartic acid (D) forms biliverdinIX δ isomer along with normal biliverdinIX α . The absorption and EPR spectra and HO catalytic activity of R183E mutant are similar to those of the wild type heme-HO complex, indicating no significant change in the active site structure with mutation. To investigate the effects of the carboxylate functionalities introduced at the position 183, we prepared R183Q, R183N, R183A, R183T, and R183Y. The HO reactions of these mutants do not produce biliverdin isomers other than the normal biliverdinIX α . These results indicate that the carboxylate group introduced at position 183 is involved in the formation of δ -biliverdin isomer. The formation of δ -biliverdin isomer is expected to result in heme rotation through

electronic repulsion between the carboxylate of E183 and heme propionate and/or change in distal side protein structure through a formation of new long-range hydrogen bond interaction network. All of the present results show the importance of the hydrogen bonding interaction between the arginine at position 183 and the carboxylates of the heme propionate group, as well as steric effect of the distal helix, for the α -regioselectivity.

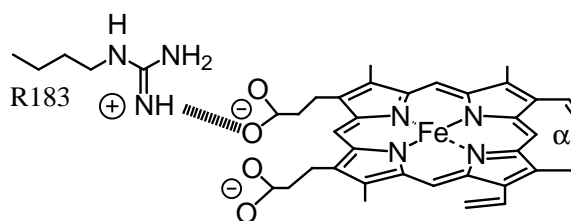


Figure 1. The hydrogen bonding interaction between R183 residue and the carboxylate of heme orients the heme to oxidize the α -meso position.

VIII-F Designing Artificial Photosynthesis at Molecular Dimensions

Photosynthesis is one of the finest piece of molecular machinery that Nature has ever created. Its ultrafast electron transfer and following well-organized sequence of chemical transformation have been, and will continue to be, challenging goals for molecular scientists. We are trying to mimic the function of photosynthesis by assembling molecular units that perform individual physical/chemical action. The molecular units include porphyrins, redox active organic molecules, and transition metal complexes.

Last year we focused our attention on developing organic reactions that utilize photoinduced electron transfer processes and are useful for synthetic organic chemistry. This is an important step toward our ultimate goal, which is to design artificial molecular systems that effect multiple chemical reactions triggered by light on the basis of molecular rationale.

VIII-F-1 Porphyrin Catalyzed Reductive Silylation and Acylation of Quinones under Irradiation of Visible Light

ITO, Hajime; NAGATA, Toshi

Considerable studies were reported for inter- or intramolecular photoinduced electron transfer from porphyrins to quinones, however, the synthetic application of a porphyrin as a photocatalyst for the reduction of quinones is thought to be still difficult. For example, when attempts to obtain the reduced products of a quinone was carried out using a porphyrin catalyst under irradiation of visible light in the presence of a proton source, no reduced products were detected. The reason for this unsuccessful result would be mainly attributed to the reverse electron transfer from a semiquinone anion radical to the porphyrin cation radical generated by the photoinduced electron transfer. If the semiquinone anion radical is chemically trapped by a silyl reagent and the successive silylation occurs, the reductive silylation product of the quinone is obtained. On the basis of this idea, we found both phenylthiotrimethylsilane (PhSTMS) and chlorotrimethylsilane (TMSCl) are a good trapping reagent for the reduced intermediate formed by photoinduced electron transfer from photo-excited porphyrins. In addition, the electrophilic substitution of a silyl sulfide with a phenoxy group releases a thiolate anion which would act as an electron donor. In the presence of a catalytic amount of porphyrin **1** (0.5 mol %), the

reductive silylation of duroquinone was proceeded under the irradiation of yellow light ($\lambda > 500$ nm) using PhSTMS to give 1,4-bis(trimethylsiloxy)-2,3,5,6-tetramethylbenzene (99%) and diphenyl disulfide (97%) in good yields. We also found that chlorotrimethylsilane (TMSCl), a more easily available silyl reagent, was also useful for the porphyrin-catalyzed reductive silylation.

Despite the reductive silylation and acylation of quinones with chlorotrimethylsilane and metal (K, Mg, Zn) were well known procedure, these methods require a stoichiometric amount of metals as a reductant and generate waste metal salt. Our method exhibit the practical advantage in view of this points. Further work on the precise mechanism for these reactions is underway.

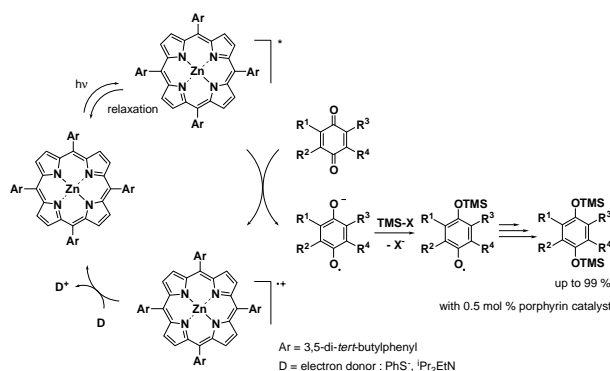


Figure 1. Porphyrin-catalyzed silylation of quinones under visible light.

VIII-G Development of New Metal Complexes as Redox Catalysts

Redox catalysis is an important field of chemistry which translates a flow of electron into chemical transformation. It is also one of the requisites for artificial photosynthesis. This project of ours aims at developing new metal complexes that perform redox catalysis at low overpotential. Our approach is to develop a series of “binary” ligands, which consist of two different types of ligands that are linked together to form metal chelates. Such ligands are particularly useful for utilizing first-row transition metal elements, because fast ligand exchange (which is often a major obstacle in studying first-row transition metal complexes in solution) is suppressed by chelate effects.

VIII-G-1 Synthesis of Terpyridine-Based Binary Ligands and Their Metal Complexes

NAGATA, Toshi; TANAKA, Koji

[*Inorg. Chem.* **39**, 3515 (2000)]

2,2':6',2''-Terpyridine is a promising ligand for application in redox catalysis, thanks to its structural

rigidity and chemical stability. Unfortunately, with first-row transition metals it easily forms homoleptic bis(terpyridine) complexes that are too stable to serve as redox catalysts. Such difficulty can be overcome by connecting a bidentate ligand to a terpyridine molecule. The “binary” ligand thus formed is potentially pentadentate and binds an octahedral metal ion leaving one vacant site for catalytic reactions. We already reported synthesis of terpyridine-catechol linked ligands and their cobalt(III) complexes (Figure 1a). Here we report synthesis of a terpyridine-salicylaldehyde linked ligand (Figure 1b) and their metal complexes.

The ligand (tpyC5NHCOsalH) was prepared by condensation of 4-(2-(5-aminopentyloxy)phenyl)-terpyridine and 2-allyloxy-3-diethoxymethyl-5-methylbenzoic acid potassium salt (prepared by 6 steps and 4 steps from commercially available material, respectively), followed by removing the allyl and diethyl acetal protecting groups (60% yield). The metal complexes ($M^{2+} = Mn^{2+}, Fe^{2+}, Co^{2+}$) were prepared by the reaction of the ligand with $[M(CH_3CN)_x](ClO_4)_2$ and 2,6-lutidine (1:1:2 in molar ratio) in CH_3CN . The ESI-MS spectra suggested 5-coordinate complexes, $[M(tpyC5NHCOsal)]^+$, were present in solutions.

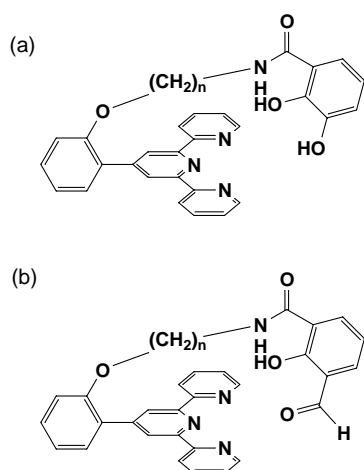


Figure 1. Terpyridine-based binary ligands.

VIII-H Development of Organic n-Type Semiconductors for Molecular Thin-Film Devices

Organic light-emitting diodes (OLEDs) and field-effect transistors (FETs) based on π -conjugated oligomers have been extensively studied as molecular thin-film devices. Organic n-type semiconductors (electron-transport materials) with low electron-injection barriers and high electron mobilities are required for highly efficient OLEDs and n-type FETs. Radical anions of an n-type semiconductor have to be generated easily at the interface with a metal electrode (electron injection), and electrons must move fast in the layer (electron mobility). Compared with organic p-type semiconductors (hole-transport materials), organic n-type semiconductors for practical use are few and rather difficult to develop. Recently, we found that perfluorinated phenylene dendrimers and oligomers are efficient electron-transport materials for OLEDs.

VIII-H-1 Synthesis, Characterization, and Electron-Transport Property of Perfluorinated Phenylene Dendrimers

SAKAMOTO, Youichi; SUZUKI, Toshiyasu; MIURA, Atsushi¹; FUJIKAWA, Hisayoshi¹; TOKITO, Shizuo¹; TAGA, Yasunori¹
(¹Toyota Central R&D Labs.)

[*J. Am. Chem. Soc.* **122**, 1832 (2000)]

Two perfluorinated phenylene dendrimers, C₆₀F₄₂ (MW = 1518) and C₁₃₂F₉₀ (MW = 3295), have been synthesized via a sequence of brominations and cross-couplings using organocopper chemistry. Two other C₆₀F₄₂ isomers containing *p*-terphenyl and *p*-quaterphenyl groups were also prepared to see structure-property relationships. Three C₆₀F₄₂s showed glass transitions at 125–135 °C. Dendrimer C₁₃₂F₉₀ melts at 426 °C and did not show a glass transition. Organic light-emitting diodes have been fabricated on indium-tin-oxide coated glass substrates by high-vacuum thermal evaporation of TPTE (a tetramer of triphenylamine) as the hole-transport layer, tris(8-quinolinolato)-aluminum as the emission layer, perfluorinated phenylenes as the electron-transport layer, LiF, and Aluminum. The maximum luminance of the device is 2860 cd/m² at 24.4 V. The electrochemical measurements indicated that the performance of the devices is improved with increasing electron affinities of the compounds. This is probably because the electron-injection barriers between the metal layers and the electron-transport layers are reduced by increased electron affinities.

VIII-H-2 Perfluorinated Oligo(*p*-Phenylene)s: Efficient n-Type Semiconductors for Organic Light-Emitting Diodes

HEIDENHAIN, Sophie; SAKAMOTO, Youichi; SUZUKI, Toshiyasu; MIURA, Atsushi¹; FUJIKAWA, Hisayoshi¹; MORI, Tomohiko¹; TOKITO, Shizuo¹; TAGA, Yasunori¹
(¹Toyota Central R&D Labs.)

[*J. Am. Chem. Soc.* in press]

Perfluorinated oligo(*p*-phenylene)s including perfluoro-*p*-quinquephenyl to -octiphenyl (PF-5P to -8P) have been synthesized by the organocopper cross-coupling method. Two PF-6P derivatives containing

trifluoromethyl and perfluoro-2-naphtyl groups were also prepared. All compounds are colorless solids and insoluble in common organic solvents. The differential scanning calorimetry measurements indicated that they are highly crystalline solids without glass transitions. Organic light-emitting diodes have been fabricated on indium-tin-oxide coated glass substrates by high-vacuum thermal evaporation of TPTE (a tetramer of triphenylamine) as the hole-transport layer, tris(8-quinolinolato)aluminum as the emission layer, a perfluorinated oligomer as the electron-transport layer, LiF, and aluminum. The electron-transport capabilities of perfluorinated oligo(*p*-phenylene)s are excellent compared with perfluorinated phenylene dendrimers. The maximum luminance of the naphthyl derivative is 19970 cd/m² at 10.0 V. The luminance-voltage and current-voltage characteristics of PF-7P and -8P are almost identical to those of PF-6P. We speculate that the electron mobility in the layer rather than the electron injection at the interface is responsible for determining the current density of PF-6P to -8P.

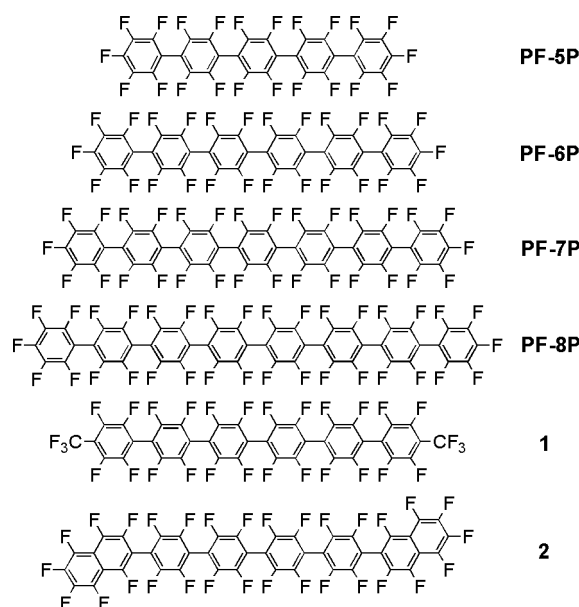


Figure 1. Perfluorinated phenylene oligomers.

VIII-I The Effects of the 2D Spin-Echo NMR Experiment on a Solid-State Homonuclear Spin-1/2 Pair

The dipolar interaction for a solid-state homonuclear spin-1/2 pair is averaged out by magic-angle sample spinning (MAS). The 2D spin-echo NMR experiment can reintroduce the influence of the homonuclear dipolar interaction into MAS powder signals.

VIII-I-1 Real Figure of Two-Dimensional Spin-Echo NMR Spectra for a Homonuclear Two-Spin System in Rotating Solids

KUWAHARA, Daisuke; NAKAI, Toshihito¹; ASHIDA, Jun²; MIYAJIMA, Seiichi
(¹Tokyo Univ. Agric. Tech.; ²Kyoto Univ.)

The 2D spin-echo NMR experiments were recently carried out on polycrystalline [2, 3-¹³C₂] L-alanine under magic-angle sample spinning (MAS) conditions, so that two unusual resonance lines emerged along the F_1 axis (*Chem. Phys. Lett.* **305**, 35 (1999)). To examine a spectral structure observed in the F_1 direction more

closely, we executed the 2D NMR experiment using a sufficiently small t_1 increment. As a result, we found many more resonance lines on a spectrum sliced off along the F_1 axis. The line distribution had a very unique and interesting structure. To elucidate the line positions theoretically, we calculated analytically the signals for the 2D spin-echo experiment performed with any t_1 increment on a homonuclear spin-1/2 pair undergoing MAS. We discovered that virtually six resonance lines (exactly twelve resonance lines) occurred on a spectrum sliced off along the F_1 axis. In addition, it was proved that the intensities of some resonance lines were largely dependent on the dipolar interaction.

VIII-J The Applications of Double-Rotation NMR Method

Double-Rotation NMR method (DOR) was applied to rare spins surrounded by abundant homonuclear spins. The application of the method to solid-state quadrupolar nuclei having $I = 1$ was investigated.

VIII-J-1 The Observation of REDOR Phenomenon for CH_x ($x \geq 2$) Spin Systems under DOR

KUWAHARA, Daisuke

Double-Rotation NMR method (DOR) was developed originally to remove second-order line broadenings for solid-state quadrupolar nuclei having half-integer spins. We applied the method to rare spins surrounded by abundant homonuclear spins (*i.e.* protons). DOR averaged out the homonuclear dipolar interactions, so that a CH_x system could be taken as an ensemble of independent CH systems. We could, therefore, detect heteronuclear dipolar interactions for CH_x ($x \geq 2$) spin systems without homonuclear decoupling techniques. In addition, we showed that DOR is also applicable to a solid-state ¹³C-¹⁴N spin pair in order to recover the heteronuclear dipolar interaction that was removed by sample spinning.

Equipment Development Center

VIII-K Development of “IMS Machines”

The technical staff of the Equipment Development Center is partly engaged in planning, researching, designing and constructing “IMS machines.” This machine, crowned with the acronym of the Institute for Molecular Science, is a high-tech experimental instrument, with emphasis on new technical idea and co-operative work with members inside and outside the Institute including those in industries. We collect suggestions of new instruments once every year from all of the members of IMS.

In this fiscal year, 1999, three project themes (1 thorough 3) were adopted as IMS machines. IMS machine projects 4 (IMS machine 1998) was completed, and project 5 (IMS machine 1998) is under way.

1. **Sorption-pump-type Large-scale Dilution Refrigerator**
(proposed by Hideo SHIBAYAMA and Takuhiko KONDOH)
2. **Vacuum-chamber-based High Voltage Application Apparatus to Fabricate Wide-range Nonlinear Optical Wavelength Converters**
(proposed by Sunao KURIMURA, Takunori TAIRA, Kazuhiro KOBAYASHI and Mitukazu SUZUI)
3. **High-speed Array Detector**
(proposed by Kazuo WATANABE and Hisashi YOSHIDA)
4. **Thin Shaped Cryostat for Opt-magnetic Measurement**
(proposed by Shinji IZUMIDA and Takuhiko KONDOH)
5. **Preparation and Transfer System for Ice-embedding Sample**
(proposed by Shinji HASEGAWA, Kazuhiro KOBAYASHI and Mitukazu SUZUI)

VIII-K-1 Vacuum-Chamber-Based High Voltage Application Apparatus to Fabricate Wide-Range Nonlinear Optical Wavelength Converters

KURIMURA, Sunao; TAIRA, Takunori; KOBAYASHI, Kazuhiro; SUZUI, Mitsukazu

This project aims at development of a vacuum-chamber-based high voltage application apparatus, which allows precise fabrication of a ferroelectric domain pattern in nonlinear optical materials. The reversal of ferroelectric spontaneous polarization is accompanied by the change of the sign of nonlinear optical coefficient, which enables quasi-phase matching (QPM) in wavelength conversion of laser light. QPM, where the period of the domain pattern corresponds to the generated wavelength in optical parametric oscillator, is an universal method to realize phase matching artificially at arbitrary wavelength (Figure 1). Periodic electrodes defined by photolithography are transferred to the domain pattern if the fidelity, affected by the atmosphere such as insulator, electrode materials, and temperature of a crystal, is reasonable (Figure 2). A widely-spread conventional technique using liquid electrodes is simple and easy, but it greatly increases the conductivity between electrodes, leading to the poor fidelity with expanded domains. While our experimental results on poling indicated the atmosphere of insulating oil and photoresist were not appropriate for high fidelity, vacuum atmosphere is an ultimate candidate to suppress surface conductivity. Temperature of the material, another important parameter, affects the domain-nucleation density and the domain wall velocity; temperature control is essential in the system. *Vacuum-based poling apparatus covering wide temperature range*, is a challenging and promising project in fabrication of QPM devices.

We so far designed the apparatus and mainly built the vacuum-related section. Requirements for this

system are summarized in Table 1. The poling system consists of three parts: a vacuum chamber, a high voltage supplier, and a temperature controlling unit. The vacuum chamber with 35 cm diameter and 32 cm height was built and high-speed vacuum pumps, a rotary pump and a diffusion pump were equipped into the system. The custom-made flanges were installed to fit the pumps with high exhaust velocity to the chamber. The carefully-checked vacuum system achieved 1×10^{-7} Torr and met our vacuum requirement in such a large chamber. It is now in the final stage of other mechanical parts assembly and will be completed at the end of this August. Another checking point was the ability of high voltage application. Since the required voltage for poling is 22000 V, which is not a low hurdle, we carefully chose shielding electric parts to meet our specification. Specially-designed flanges were provided for electric connection to fit the system. The final difficulty that we are now facing with, is in a crystal mount in a copper setting with heater and cooling pipes to stabilize the temperature. We are planning to place designed cooling pipes to obtain temperature uniformity and a sheath-shaped heater to meet the short response time as shown in Figure 4. We expect that the assembly will be finished at the end of August and total system will get ready as early as the end of September. We appreciate kind cooperation and meaningful suggestions from all related persons.

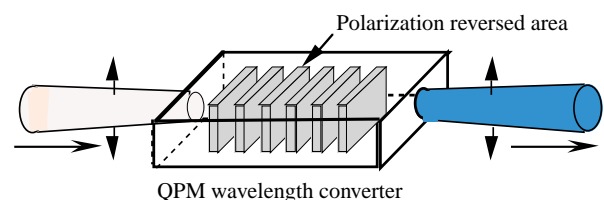


Figure 1. QPM wavelength converter to be fabricated by the vacuum-chamber-based high voltage application apparatus.

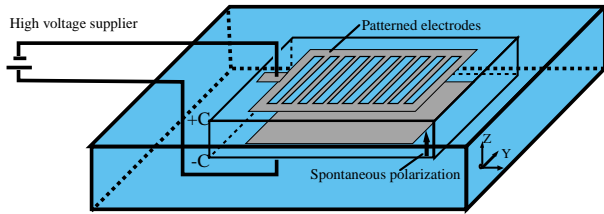


Figure 2. Fabrication method of a periodically poled QPM device.

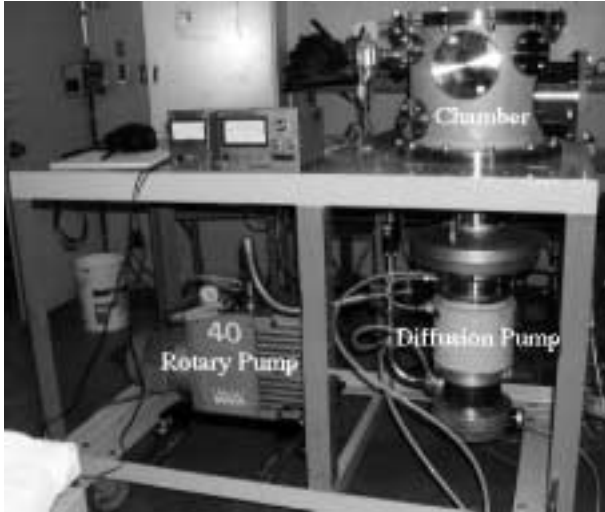


Figure 3. Overall picture of the vacuum system.

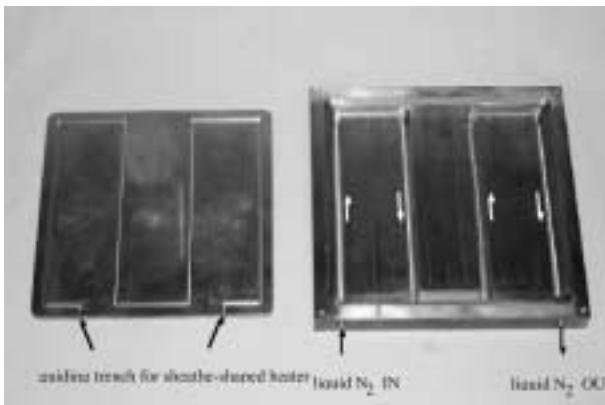


Figure 4. Crystal mount with the cooling pipes and the sheath-shaped heater. The geometry is designed to have uniform temperature distribution and short response time.

Table 1. Requirements for the apparatus.

Voltage (v)	Vacuum (Torr)	Temperature (°C)	Crystal size
24000	$10^{-3} \sim 10^{-7}$	-180 ~ 150	3 inch Φ

VIII-L Development of New Laser Materials

VIII-L-1 Deep-Ultraviolet Light Amplification within a Nanometer-Sized Layer

ASAKA, Shuji; ITOH, Minoru¹; KAMADA, Masao
(¹*Shinshu Univ.*)

Light amplification in the deep-ultraviolet region within a nanometer-sized layer is confirmed in mixed rubidium-cesium chloride crystals at room temperature. The probe laser light, which falls on the 275-nm band of Auger-free luminescence arising from radiative transition of the Cl 3p valence electrons into the Cs 5p core holes, is enhanced in intensity when the deep-lying Rb 4p core electrons are pumped into the conduction band by undulator radiation from UVSOR electron storage ring. The obtained enhancement factor roughly corresponds to an amplification coefficient of 7×10^3 /cm, which is much higher than those of typical solid-state lasers. It is emphasized that the amplification occurs in a surface layer as thin as about 20 nm, and that the inverted population between the valence and core bands is realized with any pump power. The present observation may open a new way for nanolaser fabrication.

Ultraviolet Synchrotron Orbital Radiation Facility

VIII-M Development of the UVSOR Light Source

VIII-M-1 New Lattice for UVSOR

KATOH, Masahiro; HAYASHI, Kenji; HONDA, Toru¹; HORI, Yoichiro¹; HOSAKA, Masahito; KINOSHITA, Toshio; KOUUDA, Shigeru; TAKASHIMA, Yoshifumi; YAMAZAKI, Jun-Ichiro
(¹KEK-PF)

New magnetic lattice has been designed for UVSOR. It can be realized without changing the circumference and the overall shape of the ring. An emittance of 27 nm-rad can be achieved, which is smaller by a factor of 6 than the present value. The number of straight sections will be doubled. Six straight sections will be available for insertion devices. All of them have small betatron function in vertical and are suitable for short period and narrow gap undulators, which are able to produce high brilliance soft X-rays. The new lattice has a dynamic aperture sufficiently large for injection and storage. An improvement on the main RF cavity as well as the use of the existing third harmonic RF cavity for bunch lengthening will make beam lifetime sufficiently long against strong Touschek effect.

VIII-M-2 Development of Longitudinal Feedback System for a Storage Ring Free Electron Laser

KODA, Sigeru; HOSAKA, Masahito; YAMAZAKI, Jun-Ichiro; KATOH, Masahiro; HAMA, Hiroyuki¹
(¹Tohoku Univ.)

A longitudinal feedback system for a storage ring free electron laser has been developed at the UVSOR. Instantaneous temporal deviation of the FEL optical pulse with respect to the electron bunch is measured in the frequency domain by detecting a phase between higher harmonic components of respective revolution frequencies. The phase deviation is fed back to control the storage ring rf frequency so as to readjust effective length of the optical cavity. Compensating temporal drift with the feedback system, synchronism between the FEL micropulse and the electron bunches was successfully maintained for reasonably long time.

VIII-N Researches by the USE of UVSOR

VIII-N-1 Photoelectron Spectroscopic Study on Photo-Induced Phase Transition in a Spin Crossover Complex [Fe(2-pic)₃]Cl₂EtOH

KAMADA, Masao; DOI, Yoichiro¹; FUKUI, Kazutoshi; HARUYAMA, Yuichi²; ASAKA, Shuji; TAYAGAKI, Takeshi³; YONEMURA, Naoki³; TANAKA, Kouichiro³
(¹Fukui Univ.; ²Himeji Inst. Tech.; ³Kyoto Univ.)

The purpose of the present study is to investigate the photo-induced phase transition using photoelectron spectroscopy. A single crystal of [Fe(2-pic)₃]Cl₂EtOH was grown at Kyoto university and was filed in a preparation chamber. It was found that the N-1s spectra are shifted to lower binding-energy side with cooling the sample and laser excitation causes the shift of N-1s to higher binding-energy side. The present experimental results indicate that the photo-induced phase transition of [Fe(2-pic)₃]Cl₂EtOH is closely related to both Fe and N ions and is more complicate and interesting co-operative phenomenon.

VIII-N-2 Photo-Induced Change in Semiconductor-Vacuum Interface of p-GaAs(100) Studied by Photoelectron Spectroscopy

KAMADA, Masao; MURAKAMI, Junichi¹; TANAKA, Senku²; MORÉ, Sam Dylan; ITOH, Minoru¹; FUJII, Yasuo²

(¹Shinshu Univ.; ²Osaka City Univ.)

The photo-induced change in the semiconductor-vacuum interface on GaAs (100) and Cs/GaAs(100) has been investigated with core-level photoelectron spectroscopy using synchrotron radiation and a mode-locked Nd:YAG laser. Both Ga-3d and As-3d photoelectron peaks showed transient energy shifts under the laser irradiation without any spectral change. The amounts of the energy shifts were strongly dependent on the sample temperature and the laser photon flux. It is shown that the experimental results can be fitted to a theoretical curve which was derived from the photo-induced band bending scheme in the surface layer of the semiconductor.

VIII-N-3 Excitation Spectra of a Long-Persistent Phosphor SrAl₂O₄:Eu,Dy in Vacuum Ultraviolet Region

KAMADA, Masao; MURAKAMI, Junichi¹; OHNO, Nobuhito²
(¹Shinshu Univ.; ²Osaka Electro-Commun. Univ.)

This work has been carried out to know the phosphorescence mechanism of the new-type long-persistent phosphor SrAl₂O₄:Eu,Dy. Luminescence and excitation spectra were obtained by using vacuum ultraviolet (vuv) light as excitation source. It is suggested that the 450-nm and 520-nm luminescence

bands in $\text{SrAl}_2\text{O}_4:\text{Eu,Dy}$ excited with the vuv light may be produced by a kind of host-sensitization mechanism. Creation spectrum of the long-persistent phosphorescence in the vuv region was firstly measured by observing the after-glow luminescence. A prominent peak was observed around 200 nm, namely in the low-energy tail of the fundamental absorption edge of SrAl_2O_4 . Therefore, it is suggested that the phosphorescence mechanism in $\text{SrAl}_2\text{O}_4:\text{Eu,Dy}$ may be closely related to the defect formation.

VIII-N-4 Two-Dimensional Imaging Technique for Measuring Translational Energy and Angular Distribution of Ionic Photofragments

GEJO, Tatsuo; NAKAMURA, Eiken; SHIGEMASA, Eiji; SAITO, Norio¹
(¹ETL)

During the last decade, the dynamics of molecules in the valence energy regime has been investigated by preparing excited state at well-defined energy, and analyzing photoelectron energy and angular distribution of ionic photofragments involved. Two-dimensional (2D) imaging technique is one of the most powerful tools for obtaining this information because 2D data and its simple calculation on the basis of momentum conservation law, provide Newton diagram of photofragments, which leads to dynamical process involved immediately.

The system mainly consists of an accelerator lens, a position sensitive detector (PSD) (Roendek) and an electronic system for data analysis and a computer. After the gas passes synchrotron radiation (SR) region, less than one molecule per one photon beam on the average undergoes ionization and/or dissociation. The direction of polarization of SR is parallel to the axis of TOF tube (10 cm). After the acceleration by the ion lens, ionic fragments fly through the TOF tube and hit the PSD. The determination of the impact position on the detector is based on the time delay between the two signals from each end of the wire behind the MCP. The position is obtained by the subtraction of time when both two signals arrive, providing us its velocity and direction in the center-of-mass frame. The 2D images of N_2^+ after the excitation of the valence electrons were successfully obtained. With this technique, we will try to perform the triple coincidence in the ionic fragmentation following inner-shell excitation.

VIII-N-5 Angular Distribution Measurement of Auger Electrons from Fixed in Space Molecules

GUILLEMIN, Renaud¹; SHIGEMASA, Eiji; LE

GUEN, Karine¹; CEOLINE, Denis¹; MIRON, Cataline¹; LECLERCQ, Nicola¹; UEDA, Kiyoshi²; MORIN, Paul¹; SIMON, Marc¹
(¹LURE; ²Tohoku Univ.)

[Rev. Sci. Instrum. in press]

A new experimental setup for the measurement of the angular distribution of energetically selected Auger electrons emitted from fixed in space molecules is presented. The system is based on two identical ion detectors with a small angular acceptance placed respectively at 0° and 90° of the polarization axis of the incident radiation, and a large acceptance double-toroidal electron analyzer combined with a position sensitive detection. It allows to select the molecular alignment for s and p ionization channels in parallel and provides an energy and angle measurement of the outgoing electron. The energy and angular performances as well as the calibration procedure are discussed. Samples of results obtained on the carbon monoxide ionized above the C 1s threshold are presented.

VIII-N-6 Construction of a Varied-Line-Spacing Plane Grating Monochromator at BL-4B

SHIGEMASA, Eiji; GEJO, Tatsuo

In order to realize various spectroscopic investigations in the soft X-ray region (100~1000 eV) with high resolution at UVSOR, a new Varied-line-spacing Plane Grating Monochromator (VPGM) at BL-4B was designed in 1999. The beamline is composed of two pre-focusing cylindrical mirrors (M_0 and M_1), the monochromator (M_2 and G), and a post-focusing toroidal mirror (M_3). The schematic drawing of the whole beamline is presented in Figure 1. Synchrotron radiation is deflected horizontally and focused vertically onto the entrance slit S_1 by M_0 . M_1 deflects the radiation vertically and focuses it horizontally. The radiation passing through S_1 is converged by the spherical mirror M_2 on a virtual source at a 4-m distance away from the grating center. Two varied-line-spacing plane gratings G with different groove densities (800 and 267 lines/mm) are interchangeable by a linear-translation mechanism without breaking the vacuum. The grating rotation for scanning wavelength is performed with a sine-bar mechanism. The monochromatized radiation passing through the exit slit S_2 is focused onto the sample position by toroidal mirror M_3 . The fabrication of all the optical elements and beamline components has been successfully completed and the practical construction is just beginning to be carried out.

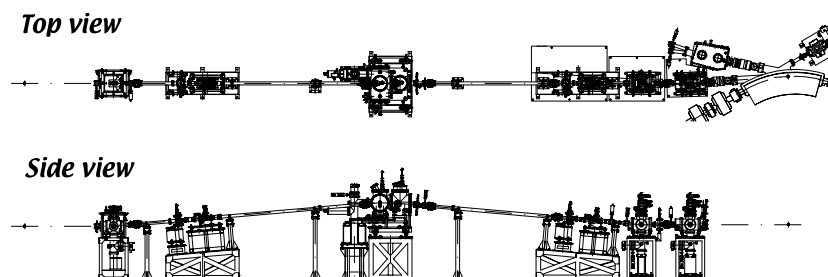


Figure 1. Schematical drawing of the VPGM on BL4B at UVSOR.

Computer Center

VIII-O Theoretical Studies on Electronic Structure and Dynamics of Electronically Excited States in Polyatomic Molecules

VIII-O-1 Theoretical Study of the Potential Energy Surfaces and Bound States of HCP

NANBU, Shinkoh; GRAY, Stephen K.¹; KINOSHITA, Tomoko; AOYAGI, Mutsumi
(¹Argonne Natl. Lab.)

[*J. Chem. Phys.* **112**, 5866 (2000)]

Global, ab initio potential energy surfaces for HCP in its ground $1^1\Sigma^+$ ($1^1A'$) and low-lying excited $1^1A''$, $2^1A'$, and $1^1\Delta$ ($2^1A''$) electronic states are determined. The multireference configuration interaction method at the double zeta with polarization basis set level is used, although some calculations augmented with diffuse functions are also discussed. Numerous quantum mechanical rovibrational states are then obtained for these surfaces, with emphasis on those corresponding to excited electronic state levels which have not been studied theoretically before. The results agree reasonably well with available experimental data for the $1^1A''$ state. Furthermore, the presence of certain local minima on the $1^1A''$ and $2^1A'$ surfaces leads to one new series of levels on the $1^1A''$ surface, and two new series on the $2^1A'$ surface.

VIII-O-2 A Comparative Study of the Quantum Dynamics and Rate Constants of the $O(^3P) + HCl$ Reaction Described by Two Potential Surfaces

SKOKOV, Sergei¹; TSUCHIDA, Tomoki¹; NANBU, Shinkoh; BOWMAN, Joel M.¹; GRAY, Stephen K.²
(¹Emory Univ.; ²Argonne Natl. Lab.)

[*J. Chem. Phys.* **113**, 227 (2000)]

Wave packet calculations, using direct and damped- L^2 real propagation methods, of initial state-resolved and cumulative reaction probabilities for the $O(^3P) + HCl$ ($1^1\Sigma^+$) \rightarrow $OH(^2\Pi) + Cl(^2P)$ reaction are reported. Results are obtained using the recently developed "S4" potential surface of Ramahandran co-workers and, for comparison, the earlier, Koizumi, Schatz and Gordon (KSG) potential energy surface. Most calculations are for total angular momentum $J = 0$, although some $J > 0$ centrifugal sudden results are also obtained. The thermal rate constant and the rate constant for HCl ($v = 1$) are obtained from the $J = 0$ cumulative reaction probability and J - K -shifting, using standard transition-state rotation constants. This type of shifting is justified by examining limited centrifugal sudden calculations. The S4 surface is shown to yield some surprising results. For example, despite a significantly higher ground state adiabatic barrier than the KSG surface, the thermal rate constant is not significantly different from one obtained with the

KSG surface, although the one for the vibrationally excited HCl is.

VIII-O-3 Determination of the Global Potential Energy Surfaces for Polyatomic Systems

NANBU, Shinkoh; ISHIDA, Toshimasa¹; GRAY, Stephen K.²; AOYAGI, Mutsumi
(¹Shizuoka Univ.; ²Argonne Natl. Lab.)

Computational algorithm of the determination of the global potential energy surfaces for polyatomic systems are developed with using the interpolant moving least squares scheme, which was proposed by Ishida and Schatz [*Chem. Phys. Lett.* **314**, 369 (1999)]. In this scheme, any derivatives in quantum-chemical calculations are not required to construct the surface and in contrast with previously developed schemes based on Shepard interpolation alone. In our new algorithm, the molecular conformations are generated with the Monte Carlo sampling, and then the ab initio calculations for all of the conformations are performed by the parallel computing at the same time. Therefore, we have good advantage for computational time for the normal calculations. Application is made to the tetra-atomic systems, the $2OH \leftrightarrow H_2O + O$ reaction.

VIII-O-4 Semiclassical Study of Nonintegrable Systems

TAKAMI, Toshiya

We study nonadiabatic processes in classically nonintegrable systems such as 2D billiards and kicked rotators to reveal essence of the dynamical characters in highly excited states of molecules. Theoretical treatment of the nonadiabatic transition between adjacent levels through an avoided crossing was studied first in pioneering works by Landau, Zener, *etc.* In the nonintegrable systems, however, the Landau-Zener formula cannot be applied because those systems contain essentially many levels, *i.e.* nonadiabatic couplings between adiabatic states cannot be ignored everywhere.

On numerical experiments in nonintegrable systems, we found non-Landau-Zener behavior, and we pointed that the phenomenon arises from nonadiabatic couplings between eigenstates on the endpoints. In order to describe the extra-transition theoretically, we introduce "boundary expansion" to get higher order terms of the nonadiabatic couplings. By the use of the expansion, we construct a new base which can describe nonadiabatic transition locally even in nonintegrable systems. This base is shown to be the same as superadiabatic base by M.V. Berry.

VIII-O-5 Development of *ab initio* MD Method Based on the Direct Evaluation of CAS-SCF Energy Derivatives**KINOSHITA, Tomoko; NANBU, Shinkoh; AOYAGI, Mutsumi**

We have been developing an *ab initio* molecular dynamics program to investigate the reaction dynamics of large scale problems, *i.e.*, surface reactions, and biological systems. Since we employed parallelized version of McMurchie-Davidson's algorithm to evaluate both AO integrals and derivatives of AO integrals, the most time consuming step of electronic structure calculations has been carried out in a tractable way. At each time steps of MD calculations, we obtain analytical energy derivatives of complete active space (CAS) wavefunctions. We continue to develop the codes for non adiabatic and spin-orbit coupling matrix elements. Our direct method can easily extend to apply a number of interesting problems including non adiabatic reactions and spin forbidden processes. For the benchmark test purposes of this program system, the low-lying singlet and triplet surfaces of $\text{CH}^+ + \text{H}_2 \leftrightarrow \text{C} + \text{H}_3^+$ is investigated by using direct *ab initio* molecular dynamics.